Epsilon-Near-Zero (ENZ)-based Optomechanics Supplementary Information

Yasaman Kiasat[1,*], Maria Grazia Donato[2,*], Michael Hinczewski[3,*], Mohamed El Kabbash[3], Theodore Letsou[3], Rosalba Saija[4,†], Onofrio Maria Maragò[2,†], Giuseppe Strangi[3,5,†], and Nader Engheta[1,†]

[1]Department of Electrical and Systems Engineering, University of Pennsylvania, Philadelphia, PA 19104, USA.
[2]CNR-IPCF, Istituto per i Processi Chimico-Fisici, I-98158 Messina, Italy.
[3]Department of Physics, Case Western Reserve University, 10600 Euclid Avenue, 44106, Cleveland, Ohio, USA.
[4]Dipartimento di Scienze Matematiche e Informatiche, Scienze Fisiche e Scienze della Terra, Università di Messina, I-98166 Messina, Italy.
[5]CNR-NANOTEC Istituto di Nanotecnologia and Department of Physics, University of Calabria, Via Pietro Bucci 87036, Rende, Italy

S1. Supplementary Methods

S1.1 Optical forces in the dipole approximation in front of epsilon-near-zero materials

Dipole approximation (DA) is an easy and quick method to calculate optical forces on a nanoparticle. It is valid when the size of the particle is very small compared to the wavelength of the field [1, 2, 3], and due to its simplicity it provides useful results that can be compared with more complex light scattering approaches (T-matrix, DDA) in the limit of small particles [4].

In DA the total optical force on a particle is usually split in a gradient force $\mathrm{F}_{\mathrm{grad}}$ and a scattering force $\mathrm{F}_{\mathrm{scat}}$ [3]:

$$\vec{\mathrm{F}}_{\mathrm{grad}}(r,z) = \frac{1}{2}\frac{n_{\mathrm{m}}}{c\varepsilon_{\mathrm{m}}}\mathrm{Re}(\alpha)\vec{\nabla}I(r,z) \tag{S 1}$$

$$\vec{\mathrm{F}}_{\mathrm{scat}}(r,z) = \frac{n_{\mathrm{m}}\sigma_{\mathrm{ext}}}{c}I(r,z)\hat{k} \tag{S 2}$$

Here, $\hat{k}$ is the wave propagation direction that for an axially directed plane wave coincides with the axial coordinate $\hat{z}$, r is the radial coordinate, c is the speed of light, $\varepsilon_{\mathrm{m}} = \varepsilon_0 n_{\mathrm{m}}^2$ is the medium permittivity, ε_0 is the vacuum permittivity, n_{m} is the refractive index of the medium, $I(r,z)$ is the wave intensity, α is the particle complex polarizability,

$$\alpha = \frac{\alpha_0}{1 - i\frac{k^3\alpha_0}{6\pi\varepsilon_{\mathrm{m}}}} \tag{S 3}$$

where α_0 is the polarizability in the static field limit (Clausius-Mossotti), and σ_{ext} is the extinction cross-section, related to the particle absorption and scattering [2, 3]:

*These authors contributed equally to this work.
†Email: rsaija@unime.it, onofrio.marago@cnr.it, gxs284@case.edu, engheta@ee.upenn.edu

$$\sigma_{\text{ext}} = \frac{k}{\varepsilon_{\text{m}}}\text{Im}(\alpha) = \sigma_{\text{abs}} + \sigma_{\text{scat}} \tag{S 4}$$

with $k = \frac{2\pi n_{\text{m}}}{\lambda}$ the wave number and λ the wavelength.

F_{grad} drives the particles towards the maximum of light intensity if they have positive polarizability; otherwise, the particles are repelled from it. On the contrary, F_{scat} always pushes the particles along field propagation direction, $\hat{k}$. Another contribution to the total force may come from the spin-curl force [3], but only when beams having spatial polarization gradients are used [5], which is not the case in this work.

Recently, it has been proposed [6] that in front of an ε-near-zero (ENZ) surface a point dipole source is subjected to a near-field repulsive force, reminding the Meissner effect in superconductors [6]. In the quasistatic approximation the near-field force is [6]:

$$\text{F}_{\text{enz}}(z) \approx -\sigma\frac{9}{512\pi^4 c}\text{Re}\left(\frac{\varepsilon_{\text{s}} - \varepsilon_{\text{m}}}{\varepsilon_{\text{s}} + \varepsilon_{\text{m}}}\right)\left(\frac{\lambda}{n_{\text{m}} z}\right)^4 P_{\text{rad}} \tag{S 5}$$

where σ is a prefactor accounting for the orientation of the dipole (σ=1, horizontal dipole; σ=2, vertical dipole), ε_{s} is the complex dielectric permittivity of the surface, z is the height of the dipole above the surface and P_{rad} is the radiated power of the dipole in free space.

S1.1.1 Plane wave illumination

Here, we calculate the total optical force on a finite-size particle in front of an arbitrary reflective surface in the dipole approximation. In this case, the exciting field E_{E} is the superposition of the incident E_I and reflected E_R electromagnetic waves which produces a standing wave that, in the simplest case of plane waves travelling in the z direction, can be written as:

$$I(z) = \frac{n_{\text{m}}\varepsilon_0 c}{2}\left|E_{\text{E}}(z)\right|^2 = \frac{n_{\text{m}}\varepsilon_0 c}{2}\left|\text{E}_0 e^{-ik(z)} + \rho\text{E}_0 e^{+ik(z)+i\phi}\right|^2 = I_0 + 2\rho I_0\cos(-2kz-\phi) + \rho^2 I_0 \tag{S 6}$$

with $I_0 = n_{\text{m}}\varepsilon_0 c E_0^2/2$. Note that z is taken positive in the direction of the reflected beam and ρ and ϕ are the amplitude and phase, respectively, of the complex reflection coefficient of the surface $r_m = \rho e^{i\phi}$, which is connected to the surface complex refraction index $\tilde{n} = n_{\text{s}} + ik_{\text{s}}$ by [7]

$$\rho = \sqrt{\frac{(n_{\text{m}} - n_{\text{s}})^2 + k_{\text{s}}^2}{(n_{\text{m}} + n_{\text{s}})^2 + k_{\text{s}}^2}} \qquad\qquad \phi = \arctan\left[\frac{-2n_{\text{m}}k_{\text{s}}}{n_{\text{m}}^2 - n_{\text{s}}^2 - k_{\text{s}}^2}\right] \tag{S 7}$$

Thus, the gradient force along the axial direction on a finite-size particle in front of a reflective surface can be written as:

$$\text{F}_{\text{grad}}(z) = \frac{1}{2}\frac{n_{\text{m}}}{c\varepsilon_{\text{m}}}\text{Re}(\alpha)\frac{dI(z)}{dz} \tag{S 8}$$

where $z = h + a$ is the axial coordinate, h is the edge-to-edge distance of the particle from the surface and a is the particle radius.

The scattering force is the sum of the opposite contributions due to the incident and reflected plane waves [8, 7, 9]:

$$\text{F}_{\text{scat}}(z) = \frac{n_{\text{m}}}{c}\sigma_{\text{ext}} I_0\left(\rho^2 - 1\right) \tag{S 9}$$

where ρ is related to the surface reflection coefficient $\left|r_m\right|^2 = \left|\rho e^{i\phi}\right|^2 = \rho^2$.

Finally, the near-field force on the particle is:

$$\text{F}_{\text{enz}}(z) \approx -\sigma\frac{9}{512\pi^4 c}\text{Re}\left(\frac{\varepsilon_{\text{s}} - \varepsilon_{\text{m}}}{\varepsilon_{\text{s}} + \varepsilon_{\text{m}}}\right)\left(\frac{\lambda}{n_{\text{m}} z}\right)^4 \sigma_{\text{scat}} I(z) \tag{S 10}$$

where the radiated power $P_{\rm rad}$=$\sigma_{\rm ext}I(z)$ is related to the light scattering process.

We can now add Eqs. S8-S10 to calculate the total optical axial force on different types of particles in front of dielectric, metallic or ENZ surfaces. As the dipole is induced by a linearly polarized wave travelling ortogonally to the surface, an horizontal dipole (σ=1 in Eq. S10) is used. We used an incident light intensity of about $5.6{\cdot}10^8$ W/m^2, corresponding to a beam power of 10 mW and a beam waist of approx. 3.5 μm, both of which can be realized in a typical experimental configuration in our laboratories. Stable equilibrium points for the particle dynamics are found at z values in which the total optical force vanishes with a negative slope. For small displacements from these points, the particles are subjected to a restoring force that can be linearized as $F_z \approx -\kappa_z z$, with κ_z the trap spring constant. We consider four types of model particles: a homogeneous dielectric (polystyrene) spherical bead, a spherical particle with parameters equivalent to an ENZ material, a spherical core-shell particle (SiO_2 core, Ag shell), and an Ag prolate spheroid. The different surfaces have been considered in the calculation by means of their complex refractive index values at 560 nm; in the ENZ case, we have chosen $n_{\rm s} \approx 0.476$ and $k_{\rm s} \approx 0.511$ in order to obtain a real part of complex permittivity close to zero and an imaginary part close to 0.5. The same values have been used for the complex permittivity of the ENZ particle.

Dielectric bead. We calculated the optical forces under λ=560 nm in water (n_m=1.33) on spherical polystyrene (relative permittivity 2.54) beads having radii a=20, 50 and 100 nm. In this case, the Clausius-Mossotti polarizability is [10]:

$$\alpha_0 = 4\pi\varepsilon_{\rm m}a^3\left(\frac{\varepsilon_{\rm p}-\varepsilon_{\rm m}}{\varepsilon_{\rm p}+2\varepsilon_{\rm m}}\right) \tag{S 11}$$

In Fig. 2a of the main text, the results (short dots) obtained in DA approximation for the 20 nm dielectric bead as a function of its distance from the different surfaces are compared with those obtained by using more sophisticated approaches (COMSOL, cicles, and T-matrix, continuous lines). A very good agreement is clearly observed. In all approaches, the total optical force on small particles is modulated by the sinusoidal term in the gradient force. It is larger (in the fN range) on more reflective surfaces and, going from Ag to ENZ, it changes phase, leading to stable traps at different distances (arrows in Fig. 2).

The axial trap spring constants $\kappa_{\rm ENZ}$ and $\kappa_{\rm Ag}$ in front of ENZ and Ag surfaces have been calculated by a linear fit of the total force at the equilibrium points. They are $\kappa_{\rm ENZ}$ = 15 fN μm^{-1} and $\kappa_{\rm Ag}$ = 27 fN μm^{-1}, that can be compared to the trap spring constant in the axial direction obtained in a standard optical tweezers setup, based on a single Gaussian beam. In this case,

$$I(x,y,z) = I_0\frac{w_0^2}{w(z)^2}\exp\left[-2\frac{x^2+y^2}{w(z)^2}\right] \tag{S 12}$$

where w_0 is the beam waist, $w(z) = w_0\sqrt{1+\frac{(z-z_0)^2}{z_R^2}}$ is the beam width at z, $z_R = \frac{n_m\pi w_0^2}{\lambda}$ is the Rayleigh range, z_0 is the position of the beam waist and $I_0 = 2P/\pi w_0^2$ is the on-axis intensity at the waist of a beam having total power P. To evaluate the beam waist, we used the Abbe criterion, $w_0 = \frac{0.5\lambda}{NA}$, with NA=1.3 the numerical aperture, as in typical single beam optical tweezers. Eqs. S1 and S2 can be used to calculate the axial component of the total force, and the corresponding k_S at the equilibrium point is obtained by a linear fit. We consider as before the particle in water and illuminated at λ=560 nm. We find, at the same light intensity used in front of ENZ and Ag surfaces, a two order of magnitude lower κ_S = 0.24 fN μm^{-1} axial spring constant.

In Fig. S1 the optical forces in DA on dielectric beads at increasing bead radius (20, 50 and 100 nm) are shown. The increasing size of the particles corresponds to larger optical forces and different trapping points. However, the 100 nm bead is not trapped in front of glass surface, whereas it is trapped in front of ENZ and Ag surfaces, whose higher reflectivity with respect glass surface better counteracts the scattering force due to the incoming beam.

In Fig. S2, a panel summarizing the results of the calculation of the total optical force (a-c) and of the near-field force (d-f) on a 20 nm dielectric bead in water is shown. Three different surfaces are considered: lossless, with medium loss (Im($\varepsilon_s/\varepsilon_0$)=0.5) and with high loss (Im($\varepsilon_s/\varepsilon_0$)=0.8). The comparison with the results obtained for a point dipole in vacuum [6] shows that in this work the presence of a medium (water) broadens the repulsive near field force region from $-1 < \varepsilon_s/\varepsilon_0 < 1$ to $-1.77 < \varepsilon_s/\varepsilon_0 < 1.77$; moreover, as

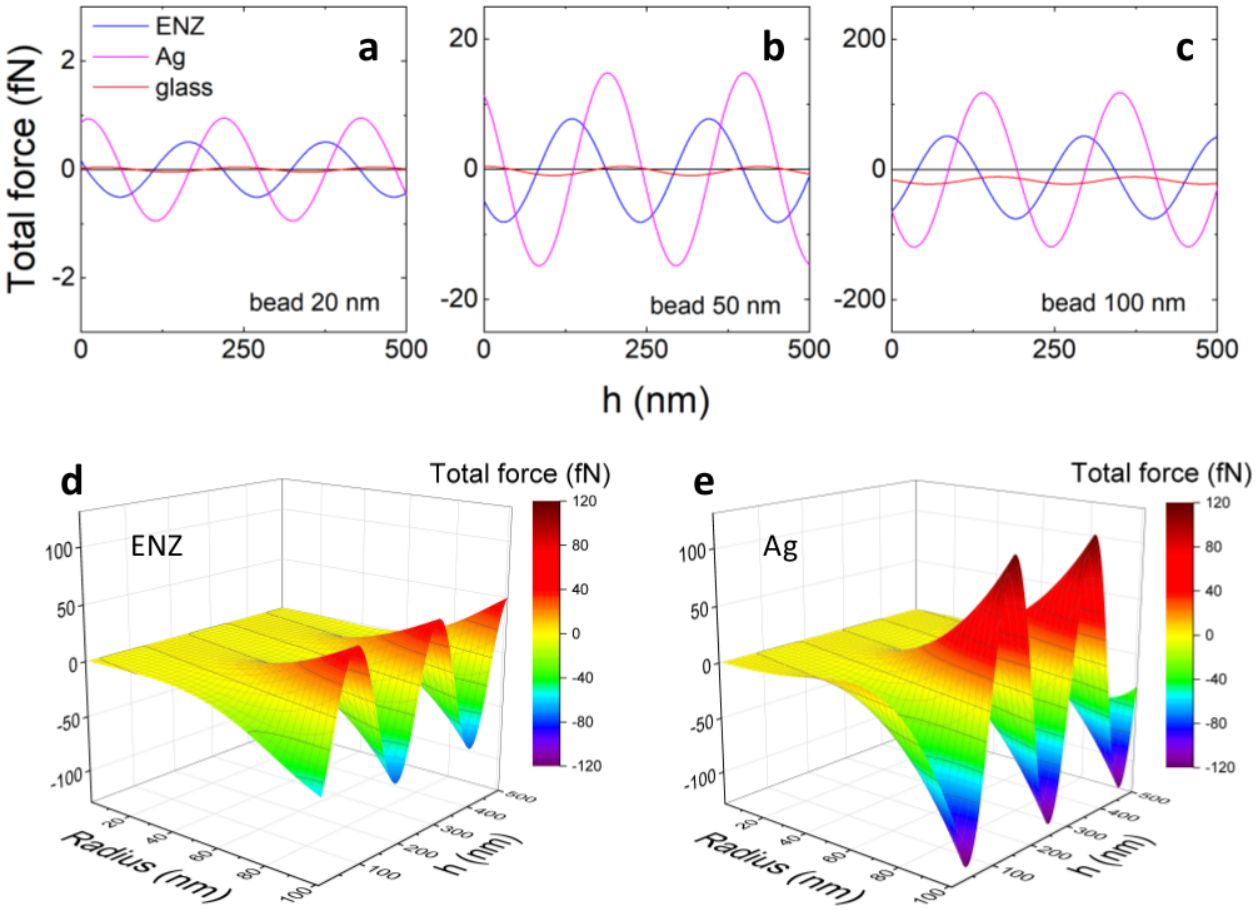

Figure S1: Optical forces on a) 20 nm, b) 50 nm and c) 100 nm radius dielectric beads. The beads are in front of ENZ (blue curve), Ag (magenta curve) or glass (red curve) surfaces. Note how for smaller particles the dominant contribution to the optical force comes from the gradient force, while for larger particles the greater scattering force shifts downwards the force modulation resulting from the interference between incident and reflected field. In d) and e), 3D plots of the total force as a function of the particle radius and of the distance from ENZ (d) and Ag (e) surfaces.

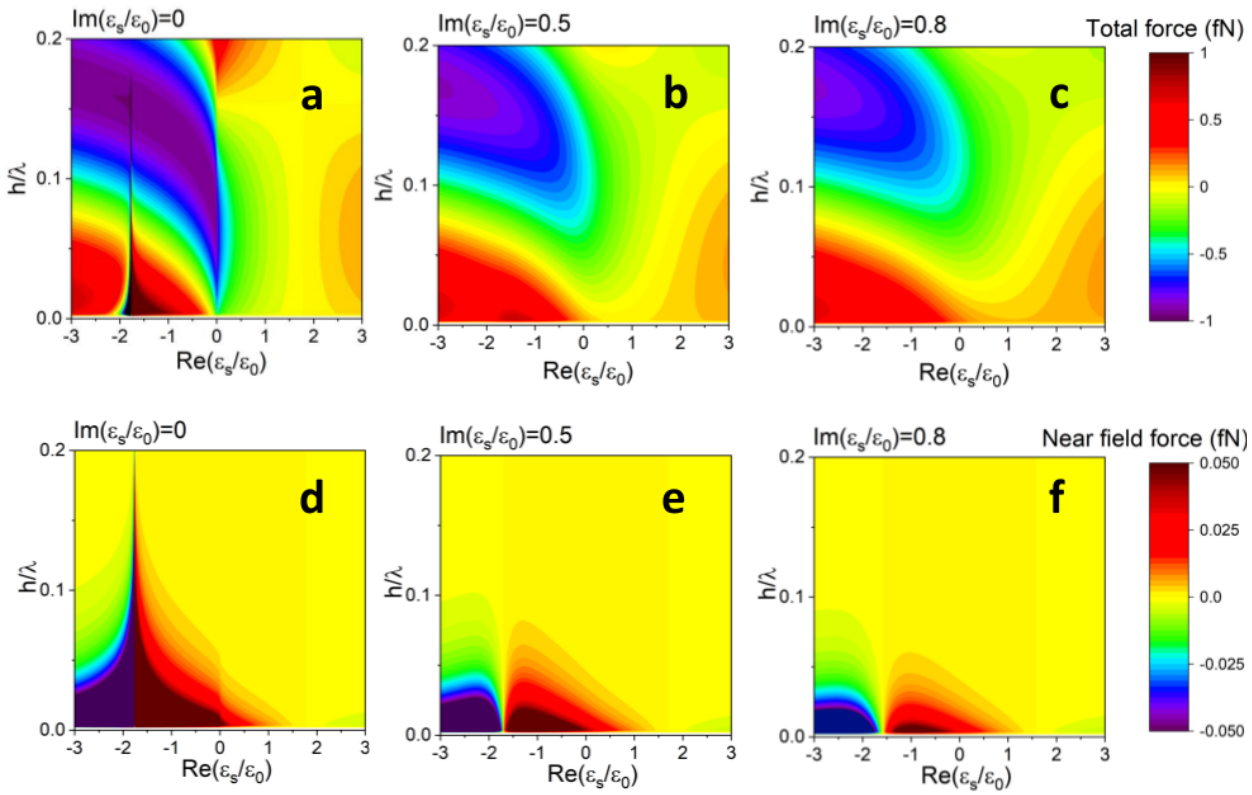

Figure S2: Contour plots of the total optical force (a-c) and of the near-field force (d-f) in front of (a,d) lossless, (b,e) medium loss, Im($\varepsilon_s/\varepsilon_0$)=0.5 and (c,f) very high loss, Im($\varepsilon_s/\varepsilon_0$)=0.8 surfaces on a 20 nm dielectric bead as a function of the real part of the surface permittivity and of the particle normalized height h/λ above the surface (λ=560 nm). The maximum optical force is in the fN range.

already observed [6], even in surfaces with high loss there is still a repulsive near field force. However, the calculation of the total optical force gives values not higher than 1 fN, which is found only in front of lossless surfaces.

Aiming at a direct comparison with Fig. 2d in Ref. [6], we plot (Fig. S3) the total and the near field forces on a 20 nm dielectric bead at h=10 nm and h=28 nm from a suface as a function of the real and imaginary part of the surface permittivity. The correspondence with results in Ref. [6] is evident, taking in account the broadening of the repulsive near field force range due to the water medium already shown in Fig. S2 (d-f).

ENZ particle. Optical forces on spherical beads made by ENZ material have been calculated in front of glass, Ag or ENZ surfaces. ENZ beads having radii a=20, 50 and 100 nm have been considered. As shown in Fig. S4, the forces are always larger than the ones observed in dielectric bead counterparts. The larger scattering force of ENZ particle hinders its trapping in front of glass surface, for all radii. Moreover, the 100 nm radius ENZ particle cannot be trapped also in front of ENZ surface (Figure S4c).

Core-shell particle. To enhance the optical force, we used a SiO_2-Ag core-shell particle designed to be resonant at approximately 560 nm and having a total radius a_{tot}= 20 nm. The calculation of the extinction cross-section shows (Fig. S5a) that the resonance condition is fulfilled if the core-shell structure has a core radius $a_1 = 16.1$ nm, and the Ag shell thickness is 3.9 nm. The particle polarizability is [10]:

$$\alpha_{cs} = 4\pi a_{tot}^3 \varepsilon_{\rm m} \frac{(\varepsilon_2 - \varepsilon_{\rm m})(\varepsilon_1 + 2\varepsilon_2) + f^3(\varepsilon_1 - \varepsilon_2)(\varepsilon_{\rm m} + 2\varepsilon_2)}{(\varepsilon_2 + 2\varepsilon_{\rm m})(\varepsilon_1 + 2\varepsilon_2) + f^3(2\varepsilon_2 - 2\varepsilon_{\rm m})(\varepsilon_1 - \varepsilon_2)} \tag{S 13}$$

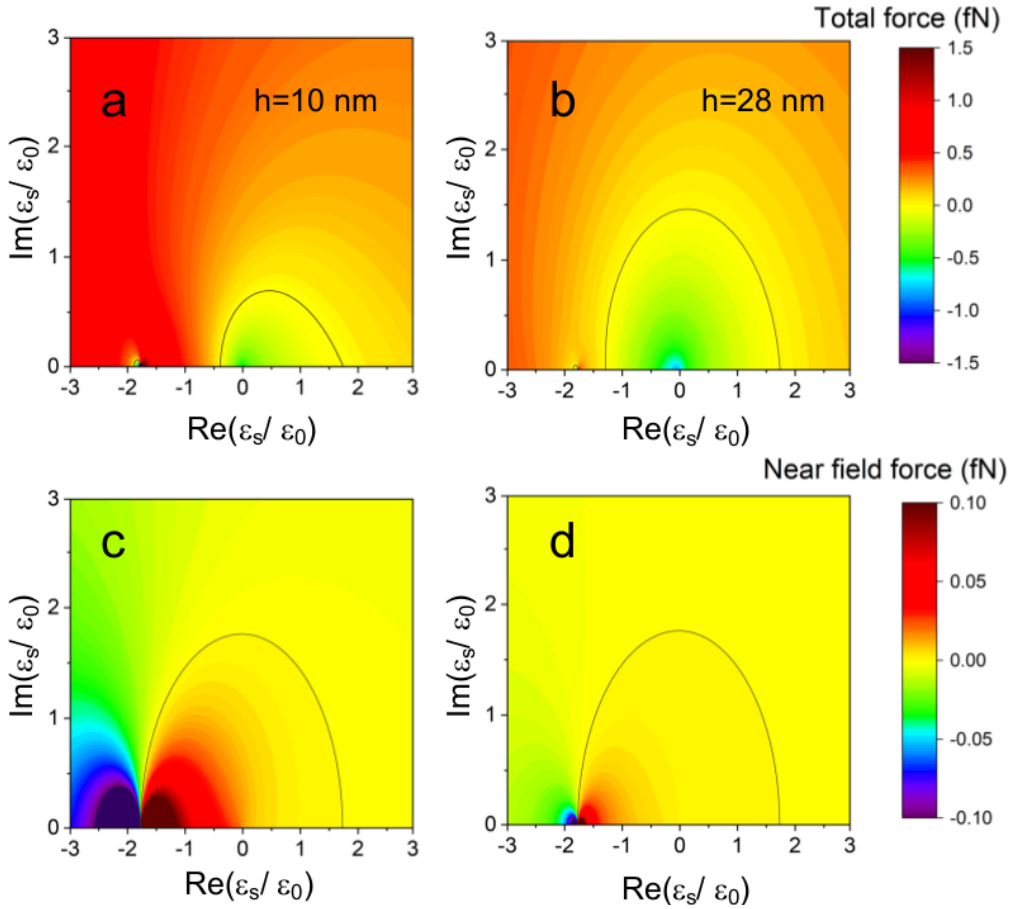

Figure S3: Contour plots of the total force (a,b) and near field force (c,d) on a 20 nm dielectric bead as a function of the real and imaginary part of the surface permittivity at h=10 nm (a,c) and h=28 nm (b,d) above the surface.

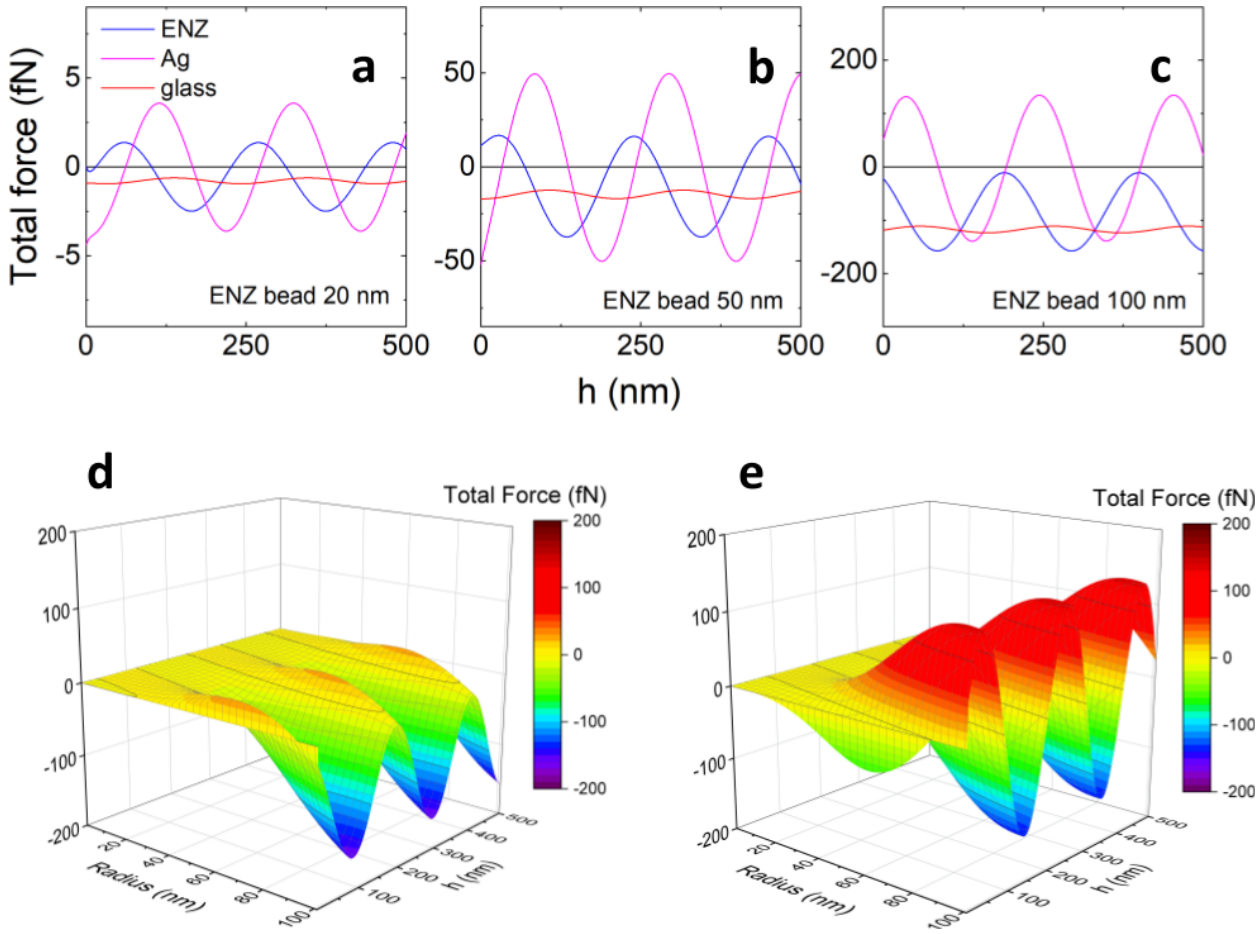

Figure S4: (a-c) Total force on spherical beads made by ENZ material. The forces are shown for 20 nm radius (a), 50 nm radius (b) and 100 nm radius (c). ENZ (blue curve), Ag (magenta) and glass (red) surfaces are considered for the calculation. (d,e) 3D plots of the total force as a function of the ENZ particle radius and of the distance from the ENZ (d) surface and Ag (e) surface.

In this equation, a_{tot} is the core-shell total radius, ε_1 and ε_2 are the core and shell complex permittivity, respectively, and $f = \frac{a_1}{a_{tot}}$ is the ratio between the core radius a_1 and the total particle radius a_{tot}.

As shown in Figure S5, the resonance at 560 nm enhances the optical force to the pN range but only at very short distances from the surfaces, being repulsive in the ENZ case and attractive in the Ag case. Otherwise, the total optical force is at the fN range.

More specifically, at the resonance $\mathrm{F_{enz}}$ is in the pN range close to the ENZ surface (from h=0 nm to roughly 10 nm). $\mathrm{F_{grad}}$ has an oscillating character, but its amplitude is smaller ($\approx$ 1 fN) than $\mathrm{F_{enz}}$, due to the small real part of the polarizability at resonance $\mathrm{Re}(\alpha) = 0.04 \cdot 10^{-32}$ Fm^2. On the contrary, $\mathrm{F_{scatt}}$ is large (tens of fN), because of the great extinction coefficient at resonance. Thus, at 560 nm (black curve in Fig. S6 a), the total force is repulsive and in the pN range close to the surface, but becomes attractive and approximately constant as the $\mathrm{F_{enz}}$ contribution fades off.

The behaviour of the forces on the core-shell particle can also be studied for wavelengths smaller and larger than the particle plasmon resonance. The calculation has been made for 552 nm, on the blue side of the plasmon resonance, and at 566 nm, on its red side. At these wavelengths, the scattering force is slightly lower than at resonance, while $\mathrm{F_{grad}}$ increase by at least one order of magnitude. For this reason, its oscillating character now can be better noticed in the total force (Fig.S6 a, blue and red curves). Moreover, as the polarizability changes sign from one side to the other of the resonance, also the gradient force is "out of phase" going from the blue to the red side of the resonance. Similar discussions hold also for the calculation of forces in front of Ag surface (Figure S6 b); however, in this case, the $\mathrm{F_{enz}}$ is attractive close to the surface.

Ag prolate spheroid. We choose an Ag prolate spheroid having long axis $a_1 = 56.8$ nm and short axes $a_2 = a_3 = 20$ nm. The particle polarizability is

$$\alpha_i = \frac{4}{3}\pi a_1 a_2 a_3 \varepsilon_{\mathrm{m}} \frac{\varepsilon_{\mathrm{p}} - \varepsilon_{\mathrm{m}}}{\varepsilon_{\mathrm{m}} + L_i(\varepsilon_{\mathrm{p}} - \varepsilon_{\mathrm{m}})} \tag{S 14}$$

In this equation, ε_{p} is the particle permittivity and L_i is a geometric factor relative to the spheroid axis a_i. In case of a prolate spheroid, L_1 is

$$L_1 = \frac{1-e^2}{e^2}\left(-1 + \frac{1}{2e}\ln\frac{1+e}{1-e}\right) \qquad\qquad e^2 = 1 - \frac{a_2^2}{a_1^2} \tag{S 15}$$

and $L_2 = L_3 = \frac{1}{2}(1 - L_1)$.

As shown in Figure S7a, the particle has, in water, a long axis resonance at 560 nm and a short axis resonance at 360 nm. For the calculation of the total optical force we considered the case in which the spheroid has the long axis aligned with the wave polarization, so to use α_1 for the polarizability in Eqs. S8 and S4, and the short semiaxis as the size parameter in Eq. S10. We obtain a further enhancement of the total optical force (tens of pN) which, as in the core-shell structure, is repulsive in front of ENZ surface and attractive in front of Ag surface. In Figure S7b a contour plot of the total optical force, calculated as a function of the surface reflectivity R and phase shift ϕ, namely, in front of all possible surfaces, is shown. We easily see that the repulsive force can be close to 200 pN in front of an "ideal" ENZ surface, having the maximum reflectivity and a vanishing phase shift.

S1.1.2 Gaussian beams

In optical tweezers, light beams are tightly focused in order to increase $\mathrm{F_{grad}}$ with respect to $\mathrm{F_{scat}}$. We can introduce this condition in our calculations by using Gaussian beams [8] instead of plane waves:

$$\mathrm{E_I}(z,r) = \mathrm{E_0}\frac{w_0}{w_i(z)}\exp\left(-\frac{r^2}{w_i^2(z)}\right)\exp\left[-ik(z+z_0) + \frac{i}{2}\frac{kr^2}{R_i} + i\arctan\left(\frac{z+z_0}{z_R}\right)\right] \tag{S 16}$$

$$\mathrm{E_R}(z,r) = \mathrm{E_0}\rho\frac{w_0}{w_r(z)}\exp\left(-\frac{r^2}{w_r^2(z)}\right)\exp\left[+ik(z-z_0) + \frac{i}{2}\frac{kr^2}{R_r} - i\arctan\left(\frac{z-z_0}{z_R}\right) + i\phi\right] \tag{S 17}$$

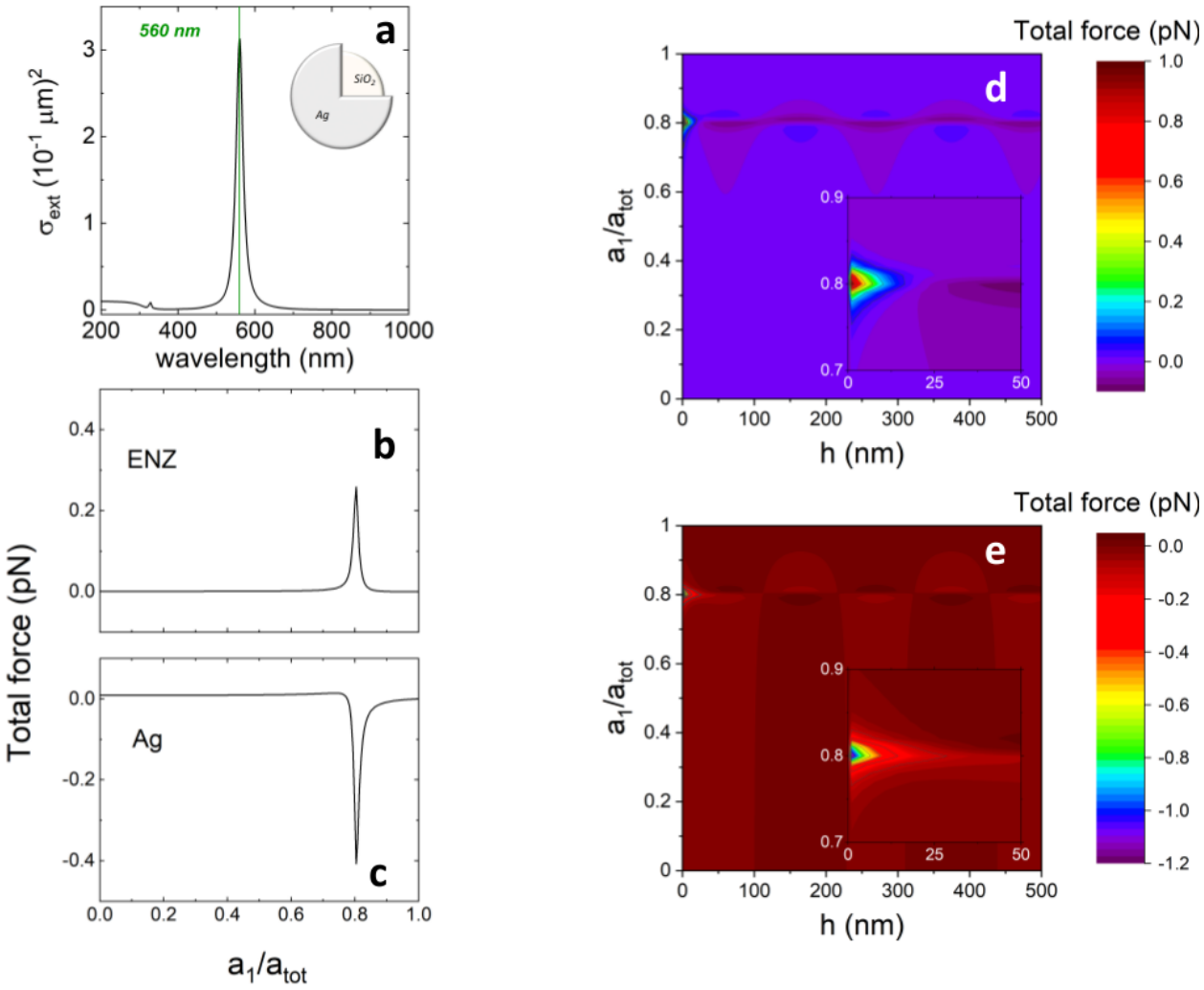

Figure S5: (a) Extinction spectrum of the SiO_2-Ag core-shell particle (total radius a_{tot}=20 nm and core radius a_1=16.1 nm) in water. (b,c) Total optical force of the core-shell particle at fixed distance h=10 nm from ENZ (b) and Ag (c) surfaces as a function of the a_1 to a_{tot} ratio. (d,e) Contour plots of the optical force with respect to the a_1 to a_{tot} ratio and the distance h from the surface. The force on the core-shell particle is in the pN range only at short distances from the surfaces and repulsive in front of ENZ (d) while attractive (e) in front of Ag.

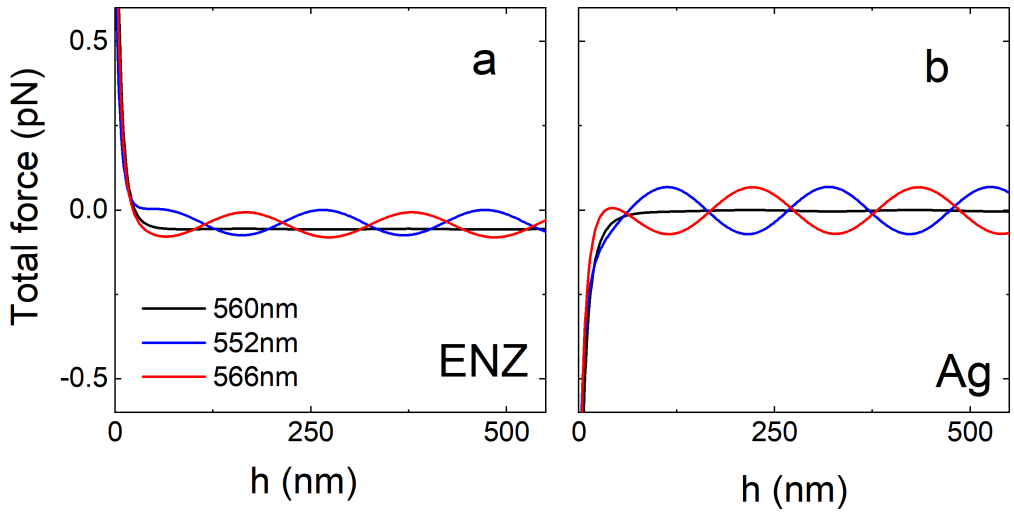

Figure S6: Total force on a SiO_2-Ag core-shell particle at three different wavelengths: at resonance (560 nm, black curve), at 552 nm (blue-shifted with respect resonance, blue curve) and at 566 nm (red-shifted with respect resonance, red curve). The total force is in the pN range close to the surface, due to the F_{enz} contribution. The sinusoidal behaviour of the gradient force is visible only out of resonance (blue and red curves), while it is negligible at resonance, where, far from the surface, only the scattering force drives the total force. Close to the surface, the total force is repulsive in front of ENZ and attractive in front of Ag.

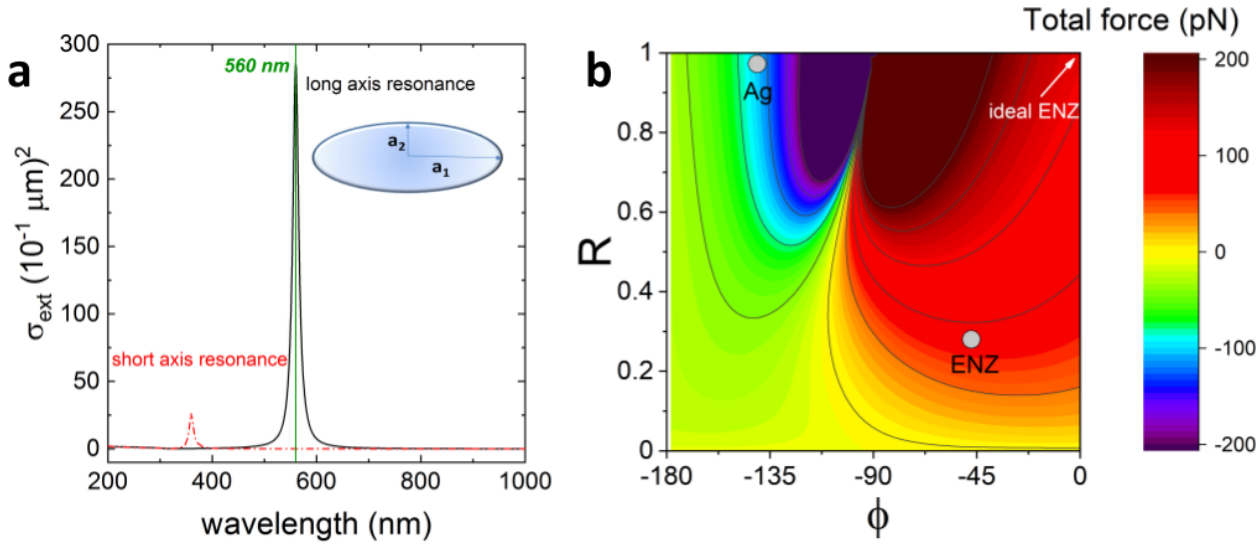

Figure S7: (a) Extinction spectra of Ag prolate ellipsoid in water oriented with the long axis parallel to the field (black solid line) and oriented with the short axis parallel to the field (red dashed line). The resonances relative to the long and short axes are indicated. (b) Contour plot of the total optical force on the Ag ellipsoid at h=10 nm distance from a surface as a function of the surface reflectivity R and phase shift ϕ. In the calculation, the spheroid is aligned with the long axis in the direction of the wave polarization. The ENZ and Ag surfaces used for the calculation of the optical forces in DA approximation are shown. The optical force is in the order of tens of pN in front of ENZ (repulsive) and Ag (attractive). The force can be close to 200 pN if the spheroid is in front of an ideal ENZ surface, having R=1 and ϕ=0.

Here, w_0 is the beam waist, $z_R = \frac{n_m \pi w_0^2}{\lambda}$ is the Rayleigh range, z_0 is the position of the beam waist, R_i and R_r are the wave curvature radii of the incident and reflected wave, respectively, and $w_i(z)$ and $w_r(z)$ are the beam widths at z distance:

$$w_i(z) = w_0\sqrt{1+\frac{(z+z_0)^2}{z_R^2}} \qquad\qquad w_r(z) = w_0\sqrt{1+\frac{(z-z_0)^2}{z_R^2}} \tag{S 18}$$

For the sake of simplicity, we restrict ourselves to the calculation of the optical force along the beam propagation axis. The light intensity distribution $I(z)$ is [8]:

$$I(z) = I_0\frac{w_0^2}{w_i^2(z)} + 2\rho I_0\frac{w_0^2}{w_i(z)w_r(z)}\cos(\psi(z)) + \rho^2 I_0\frac{w_0^2}{w_r^2(z)} \tag{S 19}$$

Here, $I_0 = 2P/\pi w_0^2$ is the on-axis intensity at the waist of a beam having total power P and

$$\psi(z) = -2kz + \arctan(\frac{z+z_0}{z_R}) + \arctan(\frac{z-z_0}{z_R}) - \phi \tag{S 20}$$

is a factor due to the phase shift of the beam on reflection from the surface. Thus, optical forces are calculated from Eqs. S1, S2 and S5.

As above, our calculations consider a particle in water (n_m=1.33) and under illumination at λ=560 nm; moreover, to evaluate the beam waist, we use the Abbe criterion $w_0 = 0.5\frac{\lambda}{NA}$, where the numerical aperture (NA) of the beam is NA=1.3, as in typical optical trapping experiments. The comparison between the results obtained with both plane wave and Gaussian beam on a small dielectric bead (radius 20 nm) are shown in Fig. S8. It is worth noting that when Gaussian beams are used, the beam power is reduced with respect to the plane wave case in order to maintain fixed the intensity at the beam focus.

S1.2 Electromagnetic scattering theory and T-matrix formalism in front of epsilon-near-zero materials

We use two different modeling approaches based on the T-matrix formalism and on finite elements methods (COMSOL), respectively. In particular, electromagnetic scattering from particles near to or deposited on a plane surface that separates two homogeneous media of different optical properties in the T-matrix formalism[11, 12, 13, 14] can give account on the role of the different multipoles in the particle-surface interaction. Indeed, the presence of the surface can have a striking effect on the scattering pattern from the particles since the exciting field does not coincide with the incident plane wave and the observed field does not coincide with the field scattered by the particle. The field that illuminates the particles is partly or totally reflected by the surface and the reflected field contributes both to the exciting and to the observed field. Moreover, the field scattered by the particles is reflected by the interface and thus contributes to the exciting field. In other words there are multiple scattering processes between the particles and the interface. As a result, the field in the accessible half-space includes the incident field $\mathbf{E}_{\mathrm{I}}$, the reflected field $\mathbf{E}_{\mathrm{R}}$, the scattered field $\mathbf{E}_{\mathrm{S}}$ and, finally, the field $\mathbf{E}_{\mathrm{SR}}$ that after scattering by the particles is reflected by the surface.

The mathematical difficulties that are met in calculating the scattering pattern are due to the need that the field in the accessible half-space satisfy the boundary conditions both across the (closed) surface of the particles and across the (infinite) interface. In other words, even by assuming that we are able to impose the boundary conditions across the surface of the particle, the problem still remains of imposing the boundary conditions across the interface[12, 13, 14]. It is possible to define the transition matrix for particles in the presence of the interface that is the starting point to calculate optical forces and torques either by direct integration of the Maxwell stress tensor or by exploiting the general expressions of optical force and torque in terms of multiple expansion[15, 16, 17].

Incident and Reflected Fields. The reflection of a plane wave on a plane surface can be dealt with in general terms, *i.e.*, without specifying whether the medium that fills the not accessible half-space is a dielectric or a metal. This information can, indeed, be supplied at the end of the algebraic manipulations. Let us thus assume that the interface is the plane $z = 0$ of a Cartesian frame of reference and that the

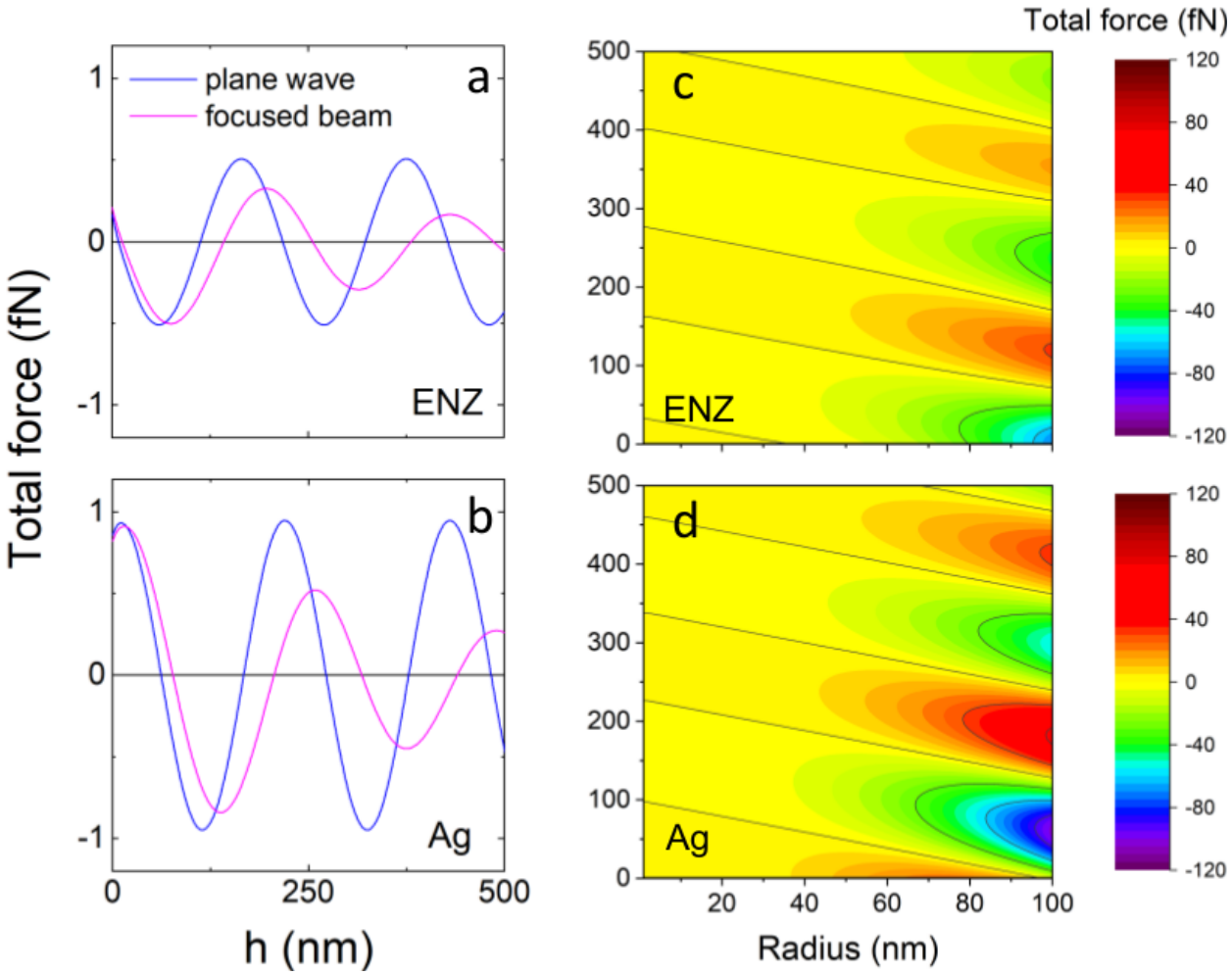

Figure S8: (a,b) Total optical force on a 20nm dielectric bead under plane wave (blue curves) and focused Gaussian beam (red curves), in front of ENZ (a) and Ag (b) surfaces, as a function of the distance h from the surface. The focusing induces a fading of the total force with h. Note that the Gaussian beam power is reduced with respect to the plane wave case in order to maintain fixed the intensity at the beam focus. (c,d) Contour plots of the total optical force on a dielectric bead under focused Gaussian beam illumination in front of ENZ (c) and Ag (d) surfaces, as a function of the distance h from the surface and of the bead radius. The modulation due to the sinusoidal term in the gradient force is clearly visible. The total force increases at increasing bead radius, reaching the range of tens of fN in front of ENZ and hundreds of fN in front of Ag surface.

half-space $z > 0$, which we take as the accessible half-space, is filled by a homogeneous medium of (real) refractive index n_m. The half-space $z < 0$ is assumed to be filled by a homogeneous medium with (possibly complex) refractive index $\tilde{n}$. Figure S9 shows the adopted geometry. The plane wave field

$$\mathbf{E}_{\mathrm{I}} = E_0 \hat{\mathbf{e}}_{\mathrm{I}} \exp(i\mathbf{k}_{\mathrm{I}} \cdot \mathbf{r}) \,, \tag{S 21}$$

which propagates within the accessible half-space, is reflected by the interface into the plane wave

$$\mathbf{E}_{\mathrm{R}} = E_0' \hat{\mathbf{e}}_{\mathrm{R}} \exp(i\mathbf{k}_{\mathrm{R}} \cdot \mathbf{r}) \,, \tag{S 22}$$

where $\mathbf{k}_{\mathrm{I}} = k'\hat{\mathbf{k}}_{\mathrm{I}}$ and $\mathbf{k}_{\mathrm{R}} = k'\hat{\mathbf{k}}_{\mathrm{R}}$ are the propagation vectors of the incident and of the reflected wave, respectively, $k' = n_m k$ and $\hat{\mathbf{e}}_{\mathrm{I}}$ and $\hat{\mathbf{e}}_{\mathrm{R}}$ are the respective unit polarization vectors. The polarization is analyzed with respect to the two pairs of unit vectors $\hat{\mathbf{u}}_{\mathrm{I}\eta}$ and $\hat{\mathbf{u}}_{\mathrm{R}\eta}$ that are parallel ($\eta = 1$) and perpendicular ($\eta = 2$) to the plane of incidence that, as usual, is defined as the plane that contains $\mathbf{k}_{\mathrm{I}}$, $\mathbf{k}_{\mathrm{R}}$ and the z axis. Our choice of the orientation is defined by the equations

$$\hat{\mathbf{u}}_{\mathrm{I}1} \times \hat{\mathbf{u}}_{\mathrm{I}2} = \hat{\mathbf{k}}_{\mathrm{I}} \,, \qquad \hat{\mathbf{u}}_{\mathrm{R}1} \times \hat{\mathbf{u}}_{\mathrm{R}2} = \hat{\mathbf{k}}_{\mathrm{R}} \,, \tag{S 23}$$

with $\hat{\mathbf{u}}_{\mathrm{I}2} \equiv \hat{\mathbf{u}}_{\mathrm{R}2}$. In terms of the projections on the polarization basis, the incident and the reflected field can be written

$$\mathbf{E}_{\mathrm{I}} = E_0 \sum_{\eta} (\hat{\mathbf{e}}_{\mathrm{I}} \cdot \hat{\mathbf{u}}_{\mathrm{I}\eta}) \hat{\mathbf{u}}_{\mathrm{I}\eta} \exp(i\mathbf{k}_{\mathrm{I}} \cdot \mathbf{r}) \,, \tag{S 24}$$

and

$$\mathbf{E}_{\mathrm{R}} = E_0' \sum_{\eta} (\hat{\mathbf{e}}_{\mathrm{R}} \cdot \hat{\mathbf{u}}_{\mathrm{R}\eta}) \hat{\mathbf{u}}_{\mathrm{R}\eta} \exp(i\mathbf{k}_{\mathrm{R}} \cdot \mathbf{r}) \,. \tag{S 25}$$

In the preceding equations the incident field $\mathbf{E}_{\mathrm{I}}$ and the reflected field $\mathbf{E}_{\mathrm{R}}$ are decomposed into their components parallel and orthogonal to the plane of incidence and can be referred to each other by means of the Fresnel coefficients F_η for the reflection of a plane wave with polarization along $\hat{\mathbf{u}}_\eta$.

Requiring the continuity of the normal and tangential components of the fields, the reflection condition[18] yields the equation

$$E_0'(\hat{\mathbf{e}}_{\mathrm{R}} \cdot \hat{\mathbf{u}}_{\mathrm{R}\eta}) = E_0 F_\eta(\vartheta_{\mathrm{I}})(\hat{\mathbf{e}}_{\mathrm{I}} \cdot \hat{\mathbf{u}}_{\mathrm{I}\eta}) \,, \tag{S 26}$$

where the Fresnel coefficients are defined as

$$F_1(\vartheta_{\mathrm{I}}) = \frac{\bar{n}^2 \cos\vartheta_{\mathrm{I}} - \left[(\bar{n}^2 - 1) + \cos^2\vartheta_{\mathrm{I}}\right]^{1/2}}{\bar{n}^2 \cos\vartheta_{\mathrm{I}} + \left[(\bar{n}^2 - 1) + \cos^2\vartheta_{\mathrm{I}}\right]^{1/2}} \,, \quad F_2(\vartheta_{\mathrm{I}}) = \frac{\cos\vartheta_{\mathrm{I}} - \left[(\bar{n}^2 - 1) + \cos^2\vartheta_{\mathrm{I}}\right]^{1/2}}{\cos\vartheta_{\mathrm{I}} + \left[(\bar{n}^2 - 1) + \cos^2\vartheta_{\mathrm{I}}\right]^{1/2}} \,, \tag{S 27}$$

in which ϑ_{I} is the angle between $\hat{\mathbf{k}}_{\mathrm{I}}$ and the z axis, $\bar{n} = \tilde{n}/n_m$. The reflected wave can be rewritten as

$$\mathbf{E}_{\mathrm{R}} = E_0 \sum_{\eta} F_\eta(\vartheta_{\mathrm{I}}) (\hat{\mathbf{e}}_{\mathrm{I}} \cdot \hat{\mathbf{u}}_{\mathrm{I}\eta}) \hat{\mathbf{u}}_{\mathrm{R}\eta} \exp(i\mathbf{k}_{\mathrm{R}} \cdot \mathbf{r}) \,. \tag{S 28}$$

The incident and the reflected field, solutions of Helmholtz equation in accessible free space, can be expanded in terms of a series of spherical vector multipole fields centered on a suitable common origin, O. To ensure the regularity of the fields at the origin, we choose J-multipole fields defined in terms of spherical radial Bessel functions $j_{\mathrm{l}}(k'r)$ [18, 11]. The result is

$$\begin{aligned} \mathbf{E}_{\mathrm{I}} &= \sum_{\eta} E_{0\eta} \sum_{plm} \mathbf{J}_{lm}^{(p)}(\mathbf{r}, k') W_{\mathrm{I}\eta lm}^{(p)} \,, \\ \mathbf{E}_{\mathrm{R}} &= \sum_{\eta} E_{0\eta} F_\eta(\vartheta_{\mathrm{I}}) \sum_{plm} \mathbf{J}_{lm}^{(p)}(\mathbf{r}, k') W_{\mathrm{R}\eta lm}^{(p)} \,, \end{aligned}$$

where the incident and reflected amplitudes are respectively:

$$W_{\mathrm{I}\eta lm}^{(p)} = W_{lm}^{(p)}(\hat{\mathbf{u}}_{\mathrm{I}\eta}, \hat{\mathbf{k}}_{\mathrm{I}}) \tag{S 29}$$

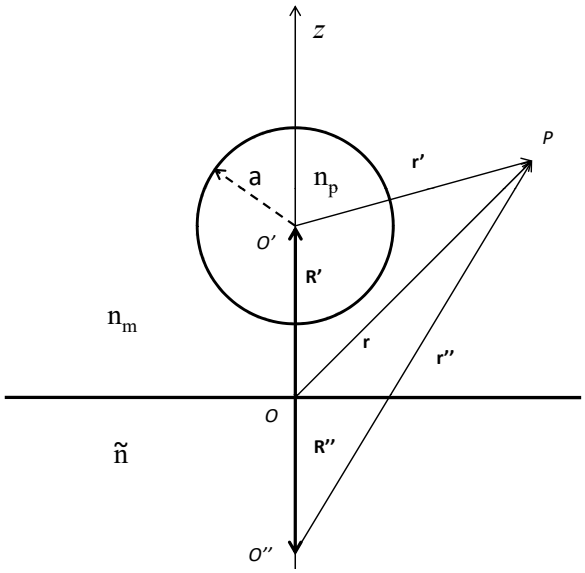

Figure S9: Geometry adopted for electromagnetic scattering from a sphere in the vicinity of a surface.

$$W^{(p)}_{\mathrm{R}\eta lm} = W^{(p)}_{lm}(\hat{\mathbf{u}}_{\mathrm{R}\eta}, \hat{\mathbf{k}}_{\mathrm{R}}). \tag{S 30}$$

Because of the reflection condition due to the presence of the surface, the incident and reflected amplitudes are not mutually independent. Infact, as the polar angles of $\hat{\mathbf{u}}_{\mathrm{R}1}$ and $\hat{\mathbf{u}}_{\mathrm{R}2}$ are

$$\vartheta_{\mathrm{R}1} = \vartheta_{\mathrm{I}} + \frac{\pi}{2}, \quad \varphi_{\mathrm{R}1} = \varphi_{\mathrm{I}} + \pi\ , \quad \text{and} \quad \vartheta_{\mathrm{R}2} = \frac{\pi}{2}, \quad \varphi_{\mathrm{R}2} = \varphi_{\mathrm{I}} + \frac{\pi}{2}\ , \tag{S 31}$$

we get

$$W^{(p)}_{\mathrm{R}\eta lm} = (-)^{\eta+p+l+m} W^{(p)}_{\mathrm{I}\eta lm}\ . \tag{S 32}$$

In this way the amplitudes of the reflected field never need to be explicitly considered, and conveniently we can define the exciting field as the superposition of incident and reflected fields

$$\mathbf{E}_{\mathrm{E}} = \mathbf{E}_{\mathrm{I}} + \mathbf{E}_{\mathrm{R}}\ . \tag{S 33}$$

As a consequence the multipole expansion of $\mathbf{E}_{\mathrm{E}}$ can be written in a more compact form as

$$\mathbf{E}_{\mathrm{E}\eta} = E_0 \sum_{plm} \mathbf{J}^{(p)}_{lm}(\mathbf{r}, k') W^{(p)}_{\mathrm{E}\eta lm} \tag{S 34}$$

with

$$W^{(p)}_{\mathrm{E}\eta lm} = [1 + F_\eta(\vartheta_{\mathrm{I}})(-)^{\eta+p+l+m}] W^{(p)}_{\mathrm{I}\eta lm}\ . \tag{S 35}$$

Scattering from a Sphere on a Plane Surface. We assume that a spherical scatterer lies entirely within the accessible half-space and is illuminated by a plane wave. Outside the scatterer the total field is

$$\mathbf{E}_{\mathrm{Ext}} = \mathbf{E}_{\mathrm{E}} + \mathbf{E}_{\mathrm{S}} + \mathbf{E}_{\mathrm{SR}}\ , \tag{S 36}$$

where $\mathbf{E}_{\mathrm{E}} = \mathbf{E}_{\mathrm{I}} + \mathbf{E}_{\mathrm{R}}$ is the same as we would have if no particle were present. $\mathbf{E}_{\mathrm{S}}$, the field scattered by the sphere, and $\mathbf{E}_{\mathrm{SR}}$, the field that after scattering by the particle is reflected by the surface, are related to each other by the reflection condition. Their superposition represent the observed scattered field that we indicate with $\mathbf{E}_{\mathrm{Obs}}$.

The field that is scattered by a sphere that lies entirely in the accessible half-space can be expanded in a series of vector H-multipole fields that satisfy the radiation condition at infinity. The multipole fields are

defined in terms of spherical radial Hankel functions[11] $h_l(k'r)$ Choosing for the scattered field the origin O' within the particle, we obtain

$$\mathbf{E}_{\mathrm{S}\eta} = E_{0\eta} \sum_{plm} \mathbf{H}^{(p)}_{S,lm}(\mathbf{r}', k') \mathcal{A}^{(p)}_{\eta lm} \ . \tag{S 37}$$

where the unknown amplitudes $\mathcal{A}$ can be determined by applying the boundary conditions at the particle's surface. The asymptotic expression of $\mathbf{E}_{\mathrm{S}\eta}$ can be written easily as follows

$$\mathbf{H}^{(p)}_{\mathrm{F}lm} = -\frac{\mathrm{i}}{4\pi k'} \frac{\mathrm{e}^{\mathrm{i}k'r'}}{r} \sum_{\eta'} \hat{\mathbf{u}}_{\mathrm{S}\eta'} W^{(p)*}_{\mathrm{S}\eta' lm} \ . \tag{S 38}$$

These are the multipole fields that enter in the definition of scattering amplitude of the system.

The scattered field $\mathbf{E}_{\mathrm{S}\eta}$ impinges on the plane surface and, by reflection yields a reflected-scattered field in the vicinity of the surface of the particle. Thanks to the reflection rule of **H**-vector multipole fields[19], that proves the fields are given by a superposition of J-multipole vector fields with origin at O', we get:

$$\mathbf{E}_{\mathrm{SR}\eta} = E_{0\eta} \sum_{plm} \sum_{p'l'} \mathbf{J}^{(p)}_{lm}(\mathbf{r}', k') \mathcal{F}^{(pp')}_{ll';m} \mathcal{A}^{(p')}_{\eta l'm} \ , \tag{S 39}$$

The quantities $\mathcal{F}^{(pp')}_{ll';m}$ can be understood as the elements of a diagonal matrix F that effects the reflection of the H-multipole fields on the plane interface giving the formal solution to the problem. Assuming that the scattering particle is a homogeneous sphere with (possibly complex) refractive index n_{p} and radius a, also the field regular at O' within the sphere can be expanded in the form

$$\mathbf{E}_{\mathrm{T}\eta} = E_{0\eta} \sum_{plm} \mathbf{J}^{(p)}_{lm}(\mathbf{r}', k_{\mathrm{p}}) \mathcal{C}^{(p)}_{\eta lm} \ . \tag{S 40}$$

The boundary conditions at the surface of the sphere between the external total field, $\mathbf{E}_{\mathrm{E}} + \mathbf{E}_{\mathrm{S}} + \mathbf{E}_{\mathrm{SR}}$, and the field within the scatterer, $\mathbf{E}_{\mathrm{T}}$, can be applied provided that the exciting field $\mathbf{E}_{\mathrm{E}}$ is referred to the center of the sphere, O'. This can be done resorting to the appropriate phase factors: $\exp(i\mathbf{k}_{\mathrm{I}} \cdot \mathbf{R}')$ and $\exp(i\mathbf{k}_{\mathrm{R}} \cdot \mathbf{R}')$. For each p, l, and m, we obtain four equations among which the amplitudes of the internal field C can be easily eliminated. As a result, we get, for each m, a system of linear nonhomogeneous equations for the amplitudes $\mathcal{A}^{(p)}_{\eta lm}$, namely

$$\sum_{p'l'} \mathcal{M}^{(pp')}_{ll';m} \mathcal{A}^{(p')}_{\eta l'm} = -\mathcal{W}^{(p)}_{\eta lm} \ , \tag{S 41}$$

where

$$\mathcal{M}^{(pp')}_{ll';m} = \left(R^{(p)}_l\right)^{-1} \delta_{pp'} \delta_{ll'} + \mathcal{F}^{(pp')}_{ll';m} \ , \tag{S 42}$$

and

$$\mathcal{W}^{(p)}_{\eta lm} = \exp(i\mathbf{k}_{\mathrm{I}} \cdot \mathbf{R}') W^{(p)}_{\mathrm{I}\eta lm} + \exp(i\mathbf{k}_{\mathrm{R}} \cdot \mathbf{R}') F_\eta W^{(p)}_{\mathrm{R}\eta lm} \ . \tag{S 43}$$

The quantities $R^{(1)}_l$ and $R^{(2)}_l$ coincide with the Mie coefficients b_l and a_l, respectively, for a homogeneous sphere of refractive index n_{p} embedded into a homogeneous medium of refractive index n_{m}. We remark that our theory can easily deal also with sphere sustaining longitudinal waves (plasmonic particles) or with radially nonhomogeneous spheres[11].

Once the amplitudes $\mathcal{A}^{(p)}_{\eta lm}$ of $\mathbf{E}_{\mathrm{S}\eta}$ have been calculated by solving (41), the reflected-scattered field $\mathbf{E}_{\mathrm{SR}\eta}$ is also determined by (45). A brief comment on the expression of the reflected-scattered field is in order. $\mathbf{E}_{\mathrm{SR}\eta}$ is valid only in the vicinity of the surface of the sphere as it includes multipole fields that do not satisfy the radiation condition at infinity, for this reason to get the reflected-scattered field that would be observed by an optical instrument in the far zone it is necessary to cast $\mathbf{E}_{\mathrm{SR}\eta}$ in its asymptotic form. At any point of the accessible half-space, $\mathbf{E}_{\mathrm{FSR}\eta}$ is given by the equation [20]

$$\mathbf{E}_{\mathrm{FSR}\eta} = E_{0\eta} \sum_{plm} \mathbf{H}^{(p)}_{FR,lm} \mathcal{A}^{(p)}_{\eta lm}, \tag{S 44}$$

where

$$\mathbf{H}^{(p)}_{\mathrm{FR},lm} = -\frac{\mathrm{i}}{4\pi k'}\frac{\mathrm{e}^{\mathrm{i}k'r''}}{r}\sum_{\eta'}\hat{\mathbf{u}}_{\mathrm{S}\eta'}W^{(p)*}_{\mathrm{S}\eta' lm}(-)^{\eta'+p+l+m}F_{\eta'}(\pi-\vartheta_{\mathrm{S}})\ . \tag{S 45}$$

for a sphere on or near the surface, this **H**-vector multipole fields with the origin at O'' can be considered as the the mirror image of the source of the original **H** fields. From the superposition of scattered and reflected-scattered fields, all referred to a common origin, eqs.37-41 and 44-45, we get the field

$$\mathbf{E}_{\mathrm{Obs}\,\eta} = E_{0\eta}\sum_{plm}\mathbf{H}^{(p)}_{\mathrm{Obs},lm}(\vec{r},k')\mathcal{A}^{(p)}_{\eta lm}\ , \tag{S 46}$$

with

$$\mathbf{H}^{(p)}_{\mathrm{Obs},lm} = -\frac{\mathrm{i}}{4\pi k'}\frac{\mathrm{e}^{\mathrm{i}k'r'}}{r}\sum_{\eta'}\hat{\mathbf{u}}_{\mathrm{S}\eta'}W^{(p)*}_{\mathrm{S}\eta' lm}[1+(-)^{\eta+p'+l+m}F_{\eta'}(\pi-\vartheta_{\mathrm{S}}] \tag{S 47}$$

Eqs. (46-47) lead us to the definition and derivation of the transition matrix for a scatterer in the presence of a plane interface[12, 13, 14]. The advantages yielded by the use of the transition matrix is evident if we had to deal with the problem of a random dispersion of non spherical particles deposited on a plane surface. Moreover, the amplitudes of the observed field are the key quantities for calculating the radiation force of which we will discuss later.

S1.2.1 Optical force in front of a substrate

In this section we briefly recall our approach to determine the radiation force exerted by a plane waves, with a definite polarization, on a scatterer (of any shape and composition) placed in a homogeneous medium of (real) refractive index n_{m}. We refer to the geometry sketched in Fig. S9 in which Σ is the customary laboratory frame and Σ' is a frame of reference whose axes are parallel to the axes of Σ and whose origin O' lies within the particle. The vector position of O' with respect to Σ is $\mathbf{R}'_O$. The conservation laws applied to the electromagnetic scattering problem leads to the optical force acting on the particle[18, 11, 3]:

$$\mathbf{F}_{\mathrm{Rad}} = r'^2\int_{\Omega'}\hat{\mathbf{r}}'\cdot\langle\mathsf{T}_{\mathrm{M}}\rangle\,\mathrm{d}\Omega'\ , \tag{S 48}$$

where the integration is over the full solid angle, r' is the radius of a sphere with center at $\vec{R}_{O'}$ surrounding the particle, and $\langle\mathsf{T}_{\mathrm{M}}\rangle$, the averaged Maxwell stress tensor (MST), describes the mechanical interaction of light with matter. The general expression of the MST in a medium in the Minkowski form[18, 11, 3] is

$$\mathsf{T}_{\mathrm{M}} = \mathbf{E}'\otimes\mathbf{D}' + \mathbf{H}'\otimes\mathbf{B}' - \frac{1}{2}\left(\mathbf{E}'\cdot\mathbf{D}' + \mathbf{H}'\cdot\mathbf{B}'\right)\mathsf{I}\ , \tag{S 49}$$

where $\mathbf{E}'$ is the electric field, $\mathbf{D}'$ is the electric displacement, $\mathbf{H}'$ is the magnetic field, $\mathbf{B}'$ is the magnetic induction, evaluated in the frame Σ' as indicated by the prime, $\otimes$ represents the dyadic product, and I is the dyadic unit. We assume that all the fields are harmonic, propagating in a homogeneous, linear, and non-dispersive medium, and depend on time through the factor $\mathrm{e}^{-i\omega t}$ that is omitted. So, we can simplify the expression for the MST by using the complex amplitudes of the fields, $\mathbf{E}' = \mathbf{E}'(\mathbf{r})$ and $\mathbf{B}' = \mathbf{B}'(\mathbf{r})$, as[21, 15, 3]:

$$\langle\mathsf{T}_{\mathrm{M}}\rangle = \frac{\varepsilon_{\mathrm{m}}}{2}\mathrm{Re}\left[\mathbf{E}'\otimes\mathbf{E}'^{*} + \frac{c^2}{n_{\mathrm{m}}^2}\mathbf{B}'\otimes\mathbf{B}'^{*} - \frac{1}{2}\left(|\mathbf{E}'|^2 + \frac{c^2}{n_{\mathrm{m}}^2}|\mathbf{B}'|^2\right)\mathsf{I}\right], \tag{S 50}$$

where the fields are the superposition of the incident and of the scattered field. In presence of a plane surface that separates two homogeneous media with different refractive indexes, the role of the incident field is played by the exciting field $\mathbf{E}_{\mathrm{E}} = \mathbf{E}_{\mathrm{I}} + \mathbf{E}_{\mathrm{R}}$ while the superposition of $\mathbf{E}_{\mathrm{S}}$ and $\mathbf{E}_{\mathrm{SR}}$ acts like the observed field due to the presence of particle. It is possible to simplify[11] equation (S 48) since the dyadic products in the expression of $\langle\mathsf{T}_{\mathrm{M}}\rangle$ give a vanishing contribution to the radiative force [21, 15]. For these reason, the component of the radiation force along the direction characterized by the unit vector $\hat{\mathbf{v}}_\zeta$ turns out to be

$$F_{\mathrm{Rad}\,\zeta} = -\frac{1}{4}\varepsilon_{\mathrm{m}}r'^2\mathrm{Re}\int_{\Omega'}(\hat{\mathbf{r}}'\cdot\hat{\mathbf{v}}_\zeta)\left[(|\mathbf{E}'_{\mathrm{Osb}}|^2 + 2\mathbf{E}'^{*}_{\mathrm{E}}\cdot\mathbf{E}'_{\mathrm{Obs}}) + \frac{c^2}{n_{\mathrm{m}}^2}(|\mathbf{B}'_{\mathrm{Obs}}|^2 + 2\mathbf{B}'^{*}_{\mathrm{E}}\cdot\mathbf{B}'_{\mathrm{Obs}})\right]\mathrm{d}\Omega'\ , \tag{S 51}$$

where $\mathbf{E}'_{\mathrm{Obs}}$ and $\mathbf{B}'_{\mathrm{Obs}}$ are the superposition of the fields scattered by the particle and the reflected-scattered fields. Obviously, since the exciting field is a plane wave, the integral (S 51) gets no contribution from the terms $\mathbf{E}'_{\mathrm{E}} \cdot \mathbf{E}'^{*}_{\mathrm{E}}$, and $\mathbf{B}'_{\mathrm{E}} \cdot \mathbf{B}'^{*}_{\mathrm{E}}$ that, accordingly, have been omitted. At this stage, using the orthogonality properties of vector spherical harmonics through which we develop the fields, see eqs. (S 34)-(S 35) and eqs.(S 37)-(S 45), we obtain the Borghese equations for the optical force components[17]:

$$F_{\mathrm{Rad}\,\zeta} = -F^{(\mathrm{Sca})}_{\mathrm{Rad}\,\zeta} + F^{(\mathrm{Ext})}_{\mathrm{Rad}\,\zeta} \tag{S 52}$$

where

$$F^{(\mathrm{Sca})}_{\mathrm{Rad}\,\zeta} = \frac{\varepsilon_{\mathrm{m}}|E_0|^2}{2k'^2}\mathrm{Re}\sum_{plm}\sum_{p'l'm'} \mathcal{A}^{(p)*}_{lm}\mathcal{A}^{(p')}_{l'm'} i^{l-l'} I^{(pp')}_{\zeta\, lml'm'} \ , \tag{S 53a}$$

$$F^{(\mathrm{Ext})}_{\mathrm{Rad}\,\zeta} = -\frac{\varepsilon_{\mathrm{m}}|E_0|^2}{2k'^2}\mathrm{Re}\sum_{plm}\sum_{p'l'm'} W^{(p)*}_{\mathrm{E}\,lm}\mathcal{A}^{(p')}_{l'm'} i^{l-l'} I^{(pp')}_{\zeta\, lml'm'} \ , \tag{S 53b}$$

where the matrix elements

$$I^{(pp')}_{\zeta\, lml'm'} = \frac{4\pi}{3}\sum_{\mu} Y^{*}_{1\mu}(\hat{\mathbf{v}}_\zeta)\frac{\mathrm{i}^{l'-l}}{16\pi^2}\sum_{\eta'}\int Y_{1\mu}(\hat{\mathbf{k}}_{\mathrm{S}}) W^{(p)}_{\mathrm{S}\eta' lm} W^{(p')*}_{\mathrm{S}\eta' l'm'}\, d\Omega_{\mathrm{S}} \ , \tag{S 54}$$

can be analytically valuated. We notice that $F^{(\mathrm{Sca})}_{\mathrm{Rad}\,\zeta}$ depends on the amplitudes $A^{(p)}_{lm}$ of the scattered field only, whereas $F^{(\mathrm{Ext})}_{\mathrm{Rad}\,\zeta}$ depends jointly on the amplitudes of the scattered field $A^{(p)}_{lm}$ and on those of the incident field $W^{(p)}_{\mathrm{I}\,lm}$. This dependence is analogous to that of the scattering cross section and of the extinction cross section, respectively, so that $F^{(\mathrm{Sca})}_{\mathrm{Rad}\,\zeta}$ can be somewhat related to scattering properties of the particle, whereas $F^{(\mathrm{Ext})}_{\mathrm{Rad}\,\zeta}$ can be related to its extinction. Similar considerations hold true also for the radiation torque [16, 22].

S1.3 Finite elements methods

To evaluate the accuracy of the analytical results, we have computed the optical force on the macro particle using numerical simulations (Fig. S10). We used software package COMSOL Multiphysics 5.4 which uses finite element method (FEM) to solve Maxwell's equation and calculate the optical force. To increase the accuracy of simulation we used periodic boundary condition; however, the micro-particle radius, a, is significantly smaller than the unit cell size, L, to prevent the mutual coupling between adjacent cells (a/L =0.02) . In order to reduce the computation time the simulation is run for silicon particle with radius a = 20 nm while the wavelength of incoming plane wave is λ=560 nm. The surrounding medium is water. We used different substrates as reflecting surfaces and compared the computed force for all substrates with the analytical results. We used silver, glass, layered structure (silver and aluminum dioxide) and ENZ surfaces. The optical properties used for all surfaces are measured values at λ=560 nm. The thickness of all substrates are considerably larger than λ to mimic the semi-infinite medium. The simulation region should be meshed finely specially in three regions: i) the plasmonic layers (Ag) in the layered structure ii) in the near-field of the substrate $(0 - \lambda/10)$ to capture the near-field effects on the calculated force and iii) the region surrounding the particle that the force is calculated.

To calculate the force, we used Maxwell's stress tensor. It is known that the total time-averaged force acting on any material objects can be found by calculating the integral of Maxwell's stress tensor on any surface that defines a volume containing the objects

$$\mathbf{F}_{\mathrm{Rad}} = \langle F(t)\rangle = \int_S \langle \mathsf{T}_{\mathrm{M}}(r,t)\rangle \cdot \hat{\mathbf{n}}\ dS \tag{S 55}$$

where T_{M} is the Maxwell's stress tensor calculated based on the total electric and magnetic fields, S is the surface surrounding the volume containing the object and $\hat{\mathbf{n}}$ is the unit vector perpendicular to the surface S. In the simulation, we chose a cylinder as a surrounding volume (Fig. S10b). In our simulation, we are interested to calculate the force in z direction consequently $\langle \mathsf{T}_{\mathrm{M},zz}(r,t)\rangle$ on top and bottom of the

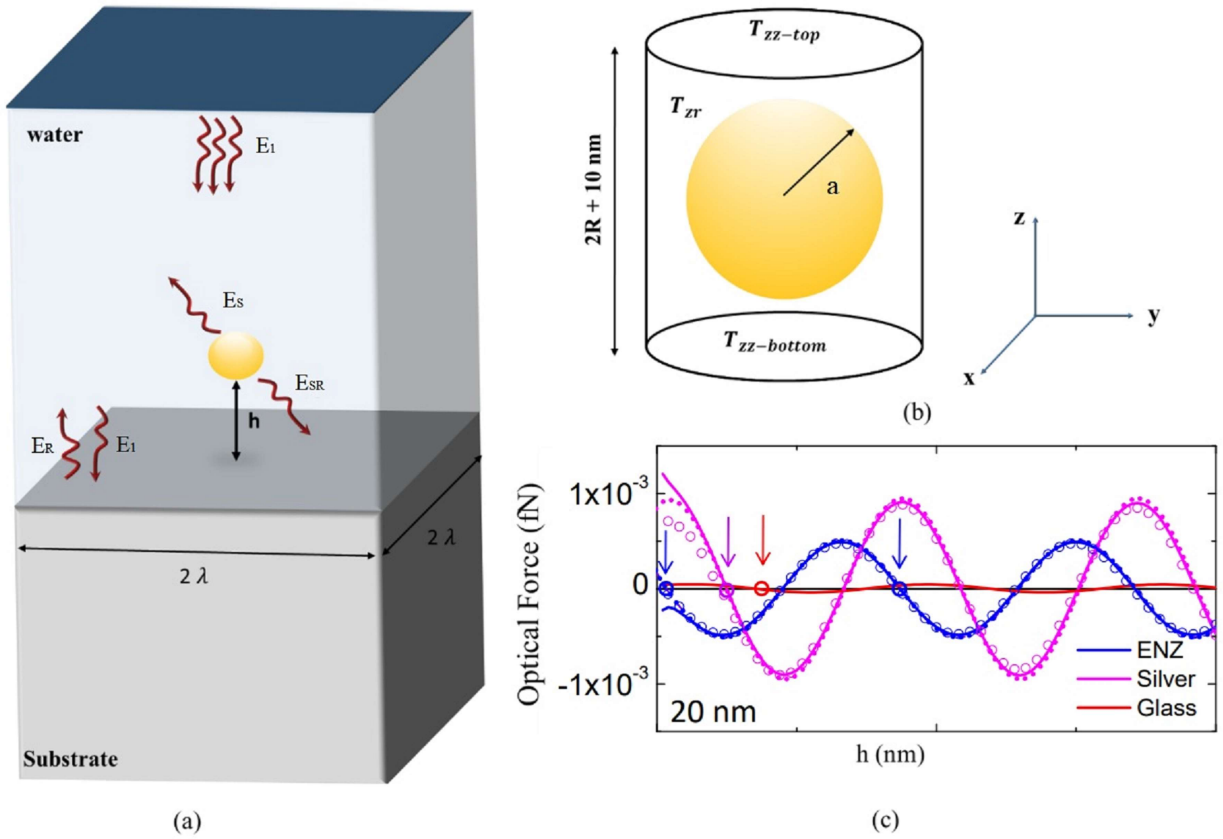

Figure S10: Numerical computation of the optical force: (a) Simulation region and the geometry of the problem. A polystyrene particle is placed above a substrate, the distance h is from the bottom of the particle to the substrate. The particle is surrounded with water and the incoming plane-wave is illuminated from the top and propagates in –z direction. (b) Calculation of the optical force by integration of Maxwell's stress tensor on a surface of cylindrical volume surrounding the particle. The Maxwell's stress tensor consists of information about the total electric and magnetic field which includes incident field (E_{I}), reflected field (E_{R}), field scattered by the particle due to the excitation filed (E_{S}), and field scattered by the particle and reflected by the surface (E_{RS}). As we are interested on the optical force in z direction it is enough to integrate $\mathsf{T}_{\mathrm{M},zz}$ on top and bottom surface and $\mathsf{T}_{\mathrm{M},rz}$ on the circumferential surface. (c) [Fig. 2a of the main text] Numerical computation (circles) versus analytical T-matrix calculation (solid line) and dipole approximation calculation (dots) of optical force for different distances h above different substrates (Silver, ENZ, glass).

cylinder and $\langle T_{zr}(r,t)\rangle$ on its circumference should be calculated (Fig. S10b). As the normal vector on the top and bottom of the cylinder has opposite direction, the total time-averaged force is:

$$\langle F(t)\rangle = \int_{S_{Top}} \langle \mathsf{T}_{\mathrm{M},zz}(r,t)\rangle dS - \int_{S_{Bottom}} \langle \mathsf{T}_{\mathrm{M},zz}(r,t)\rangle dS + \int_{S_{Circum}} \langle \mathsf{T}_{\mathrm{M},rz}(r,t)\rangle dS \tag{S 56}$$

As integrals in Eq. S56 are calculated over the surface of the cylinder, the cylinder is meshed densely ($\lambda/200$) to avoid the numerical error. Since the field scattered by the particle causes no singularity, the height and radius of the cylinder can be as close as possible to the diameter and radius of the sphere respectively, however the smaller is the cylinder the denser should be the mesh to capture the intensity of the electric and magnetic field. To avoid computational error within reasonable computation time, the height of the cylinder is chosen to be 10 nm bigger than the sphere's diameter and the radius of the cylinder to be 5 nm bigger than the radius of the sphere. The numerical computation of total force is done for various spacing (h) of the sphere from different reflecting surfaces (Fig. S10a). h is the distance from the bottom of the sphere to the surface as shown in Fig. S10a. The numerical calculation is done for several scenarios; various spacing h, various radii a, different substrates, and particles with different polarizabilities and geometries. The comparison between analytical solution and numerical analysis for various spacing above various substrates is shown in Fig. 2a. There is a very good agreement between analytical calculation and numerical simulation.

S1.4 Layered metamaterial calculations

Transfer matrix numerical details. The numerical results in Fig. 3 of the main text for reflectance (R) versus reflected phase (ϕ) from the surface of a thin film stack at constant wavelength $\lambda = 560$ nm, as described in the caption, are calculated using the standard transfer matrix approach [23]. The dependence of the phase on wavelength for a subset of the stack configurations in main text Fig. 3 is shown in Fig. S11. The refractive indices at 560 nm for each material are as follows: Ag: $0.146+3.27i$ [24]; Al_2O_3: 1.68 [25]; Au: $0.384 + 2.55i$ [24]; Ge: $3.02 + 2.90i$ [26]; TiO_2: 2.43 [27]; glass substrate: 1.52; water superstrate: 1.33 [28].

Experimental comparison. The experimental (ϕ, R) points shown as green stars in Fig. 3 are based on six different fabricated trilayer thin film stack systems (5 trilayers of Al_2O_3 / Ag / Ge from top to bottom). The Ag layer thicknesses were in the range 10-25 nm, with a thin Ge layer (1-3 nm) underneath to ensure surface wetting. The Al_2O_3 thicknesses were systematically varied between roughly 20 nm and 80 nm across the different systems. These stacks were deposited on a glass substrate (Corning Inc.) using electron-beam evaporation for Ge (0.5 Å/s) and Al_2O_3 (0.3 Å/s), and thermal evaporation for Ag (0.5 Å/s). All materials were purchased from Kurt J. Lesker. The sample's ellipsometric properties (amplitude Ψ and phase difference Δ) were measured in an air superstrate using a Variable-angle, high-resolution spectroscopic ellipsometer (J. A. Woollam Co., Inc, V-VASE) for incident angles 45°, 50°, 55° and wavelength range $300 - 1000$ nm. Individual fits to the ellipsometric data for each system yielded best-fit results for the thicknesses and optical constants, which were then used to estimate the values of R and ϕ at normal incidence with $\lambda = 560$ nm shown in Fig. 3.

Effective medium theory. The effective medium theory (EMT) used to calculate the (ϕ, R) curves in Fig. 1c and the curve labeled EMT in Fig. 3 takes the following form. We consider the interface between a water superstrate with refractive index n_0 and an underlying metamaterial which is a mixture of dielectric with index n_d and a metal with complex index $\tilde{n}_{\mathrm{M}} = n_{\mathrm{M}} + ik_{\mathrm{M}}$. If f is the filling fraction of the metal versus the dielectric, the approximate EMT permittivity of the metamaterial is given by $\epsilon_{\mathrm{EMT}} = (1-f)n_d^2 + f\tilde{n}_{\mathrm{M}}^2$. This allows us to calculate the effective refractive index n_{EMT} and extinction coefficient k_{EMT} as:

$$n_{\mathrm{EMT}} = \sqrt{\frac{|\epsilon_{\mathrm{EMT}}| + \mathrm{Re}\,\epsilon_{\mathrm{EMT}}}{2}}, \quad k_{\mathrm{EMT}} = \sqrt{\frac{|\epsilon_{\mathrm{EMT}}| - \mathrm{Re}\,\epsilon_{\mathrm{EMT}}}{2}}. \tag{S 57}$$

The corresponding complex Fresnel reflection coefficient is given by:

$$r_{\mathrm{EMT}} = \frac{n_0 - n_{\mathrm{EMT}} - ik_{\mathrm{EMT}}}{n_0 + n_{\mathrm{EMT}} + ik_{\mathrm{EMT}}}. \tag{S 58}$$

The associated reflectance $R = |r_{\mathrm{EMT}}|^2$ and phase $\phi = -\arg r_{\mathrm{EMT}}$.

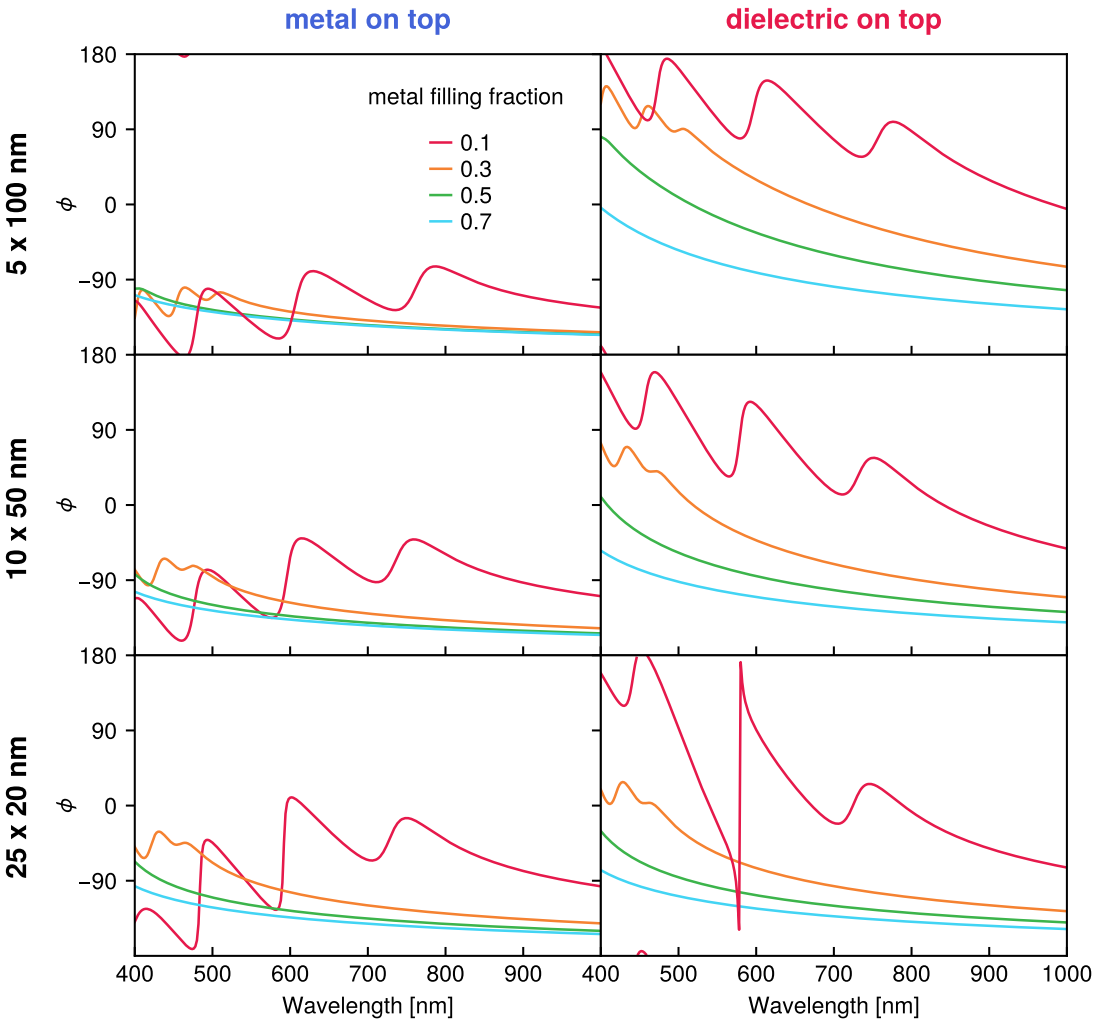

Figure S11: The dependence of phase ϕ versus wavelength for a subset of the layered metamaterials shown in main text Fig. 3, calculated using the transfer matrix approach. The three rows are labeled $n \times d$, where n refers to the number of bilayers in the stack, and d the thickness of each bilayer. The total thickness $nd = 500$ nm is kept constant. The bilayers consist of individual Ag and Al_2O_3 layers, with the fraction of Ag in the bilayer indicated by the metal filling fraction color. The left column corresponds to systems where the metal is the upper layer in each bilayer (the one closest to the surface), while the right column corresponds to the ones where the dielectric is on top.

S2. Supplementary Discussion

S2.1 Casimir effect

Casimir effect is usually observed between two metallic surfaces (or a particle and a surface) at very short distances and usually for large (μm-size) particles. In the case of dielectric beads, the Casimir force is even weaker. More in detail, literature studies of Casimir forces in liquids are outlined in the following. Munday et al. [29] consider 40 μm PS bead coated with Au layer in front of a Au plate in ethanol. They show a maximum Casimir force of approximately 800 pN at less than 30 nm from the plate, that decays at 10 pN at 100 nm from the plate. Munday et al., [30] consider 40 μm PS bead coated with Au layer in front of a silica or Au plate in bromobenzene. They show attractive or repulsive Casimir forces, whose maximum values are 150 pN at 20 nm from the plate, decaying at 1 pN at approximately 100 nm from the plate. Le Cunuder et al. [31] used a 75 microns PS bead Au coated in front of an Au plate in N_2 atmosphere and in ethanol: in the first case, the measured Casimir force is approximately 150 pN at 100 nm from the surface, while in ethanol they confirm the result of Ref. [29] measuring a larger Casimir force (1400 pN), but with a larger bead. Finally, L.B. Pires et al. [32] measured the Casimir force between two PS beads having radii R_1=2 μm and R_2=11 μm in water. The maximum Casimir force is between 5 and 10 fN at a distance between 400 nm and 500 nm, but vanishes before reaching 1mm.

We now compare these results with our particles. In the case of the Ag ellipsoid, we can consider the equivalent sphere, which should have approximately a radius of 28 nm. In this case a linear scaling [33] of the Casimir force with the particle size (from 40 μm to 30 nm) should give a value slightly lower than 0.8 pN if we consider a metallic surface and Ref. [29], or even less if we consider Ref. [30]. As shown in Fig. 4f of our paper, the total force on the Ag ellipsoid in front of Ag or ENZ is approx. 0.2 nN, so we can safely neglect the Casimir force contribution. In the case of the 20 nm core-shell particle, the Casimir force should be, according to Ref. [29], 0.4 pN or even less (0.08 pN if we consider Ref. [30]). As shown in Fig. 4e of the paper, the total force is in the pN range, so we could neglect the Casimir contribution, as in the Ag ellipsoid case, but with a slightly larger error. In the case of the 20 nm dielectric bead, we can refer to Ref. [32], giving a Casimir force (scaling the force with the particle size) between 0.05 and 0.1 fN, the latter in the best case. Again, the total force we obtain (Fig. 2a) for a 20 nm dielectric bead in water in front of Ag or ENZ surfaces is in the fN range, so we think that also in this case the Casimir force contribution could be neglected.

Supplementary References

[1] P. C. Chaumet and M. Nieto-Vesperinas, "Time-averaged total force on a dipolar sphere in an electromagnetic field," *Optics Letters*, vol. 25, pp. 1065–1067, 2000.

[2] J. Arias-González and M. Nieto-Vesperinas, "Optical forces on small particles: attractive and repulsive nature and plasmon-resonance conditions," *Journal of the Optical Society of America A*, vol. 20, pp. 1201–1209, JUL 2003.

[3] P. H. Jones, O. M. Maragò, and G. Volpe, *Optical tweezers: Principles and applications.* Cambridge: Cambridge University Press, 2015.

[4] P. Polimeno, A. Magazzù, M. A. Iatì, F. Patti, R. Saija, C. Degli Esposti Boschi, M. G. Donato, P. G. Gucciardi, P. H. Jones, G. Volpe, and O. M. Maragò, "Optical tweezers and their applications," *Journal of Quantitative Spectroscopy & Radiative Transfer*, vol. 218, pp. 131–150, 2018.

[5] O. M. Maragò, P. H. Jones, P. G. Gucciardi, G. Volpe, and A. C. Ferrari, "Optical trapping and manipulation of nanostructures," *Nature Nanotechnology*, vol. 8, pp. 807–819, 2013.

[6] F. J. Rodríguez-Fortuño, A. Vakil, and N. Engheta, "Electric levitation using epsilon-near-zero metamaterials," *Physical Review Letters*, vol. 112, no. 3, p. 033902, 2014.

[7] M. Born and E. Wolf, *Principles of Optics, 6th ed.* Pergamon, Tarrytown, NY, 1980.

[8] P. Zemánek, A. Jonáš, L. Šrámek, and M. Liška, "Optical trapping of Rayleigh particles using a Gaussian standing wave," *Optics Communications*, vol. 151, pp. 273–285, 1998.

[9] W. N. Hansen, "Electric fields produced by the propagation of plane coherent electromagnetic radiation in a stratified medium," *Journal of the Optical Society of America*, vol. 58, no. 3, pp. 380–390, 1968.

[10] C. F. Bohren and D. R. Huffman, *Absorption and scattering of light by small particles.* John Wiley & Sons, 1998.

[11] F. Borghese, P. Denti, and R. Saija, *Scattering from Model Nonspherical Particles.* Berlin: Springer, 2007.

[12] F. Borghese, P. Denti, R. Saija, E. Fucile, and O. Sindoni, "Optical properties of model anisotropic particles on or near a perfectly reflecting surface," *Journal of the Optical Society of America A*, vol. 12, no. 3, pp. 530–540, 1995.

[13] P. Denti, F. Borghese, R. Saija, E. Fucile, and O. Sindoni, "Optical properties of aggregated spheres in the vicinity of a plane surface," *Journal of the Optical Society of America A*, vol. 16, no. 1, pp. 167–175, 1999.

[14] P. Denti, F. Borghese, R. Saija, M. A. Iatı', and O. I. Sindoni, "Optical properties of a dispersion of randomly oriented identical aggregates of spheres deposited on a plane surface," *Applied Optics*, vol. 38, no. 30, pp. 6421–6430, 1999.

[15] R. Saija, M. A. Iatì, A. Giusto, P. Denti, and F. Borghese, "Transverse components of the radiation force on nonspherical particles in the t-matrix formalism," *Journal of Quantitative Spectroscopy and Radiative Transfer*, vol. 94, pp. 163 – 179, 2005.

[16] F. Borghese, P. Denti, R. Saija, and M. A. Iatì, "Radiation torque on nonspherical particles in the transition matrix formalism," *Optics Express*, vol. 14, pp. 9508–9521, 2006.

[17] F. Borghese, P. Denti, R. Saija, and M. A. Iatì, "Optical trapping of nonspherical particles in the T-matrix formalism," *Optics Express*, vol. 15, pp. 11984–11998, 2007.

[18] J. D. Jackson, *Classical Electrodynamics.* New York: J. Willey & Sons, 1999.

[19] E. Fucile, F. Borghese, P. Denti, R. Saija, and O. Sindoni, "General reflection rule for electromagnetic multipole fields on a plane interface," *IEEE Transactions on Antennas and Propagation*, vol. 45, no. 5, pp. 868–875, 1997.

[20] T. Wriedt and A. Doicu, "Light scattering from a particle on or near a surface," *Optics Communications*, vol. 152, no. 4-6, pp. 376–384, 1998.

[21] M. I. Mishchenko, "Radiation force caused by scattering, absorption, and emission of light by non-spherical particles," *Journal of Quantitative Spectroscopy and Radiative Transfer*, vol. 70, pp. 811–816, 2001.

[22] P. L. Marston and J. H. Crichton, "Radiation torque on a sphere caused by a circularly-polarized electromagnetic wave," *Physical Review A*, vol. 30, no. 5, p. 2508, 1984.

[23] J. Chilwell and I. Hodgkinson, "Thin-films field-transfer matrix theory of planar multilayer waveguides and reflection from prism-loaded waveguides," *Journal of the Optical Society of America A*, vol. 1, no. 7, pp. 742–753, 1984.

[24] A. D. Rakić, A. B. Djurišić, J. M. Elazar, and M. L. Majewski, "Optical properties of metallic films for vertical-cavity optoelectronic devices," *Applied Optics*, vol. 37, no. 22, pp. 5271–5283, 1998.

[25] R. Boidin, T. Halenkovič, V. Nazabal, L. Beneš, and P. Němec, "Pulsed laser deposited alumina thin films," *Ceramics International*, vol. 42, no. 1, pp. 1177–1182, 2016.

[26] T. Amotchkina, M. Trubetskov, D. Hahner, and V. Pervak, "Characterization of e-beam evaporated Ge, YbF_3, ZnS, and LaF_3 thin films for laser-oriented coatings," *Applied Optics*, vol. 59, no. 5, pp. A40–A47, 2020.

[27] T. Siefke, S. Kroker, K. Pfeiffer, O. Puffky, K. Dietrich, D. Franta, I. Ohlídal, A. Szeghalmi, E.-B. Kley, and A. Tünnermann, "Materials pushing the application limits of wire grid polarizers further into the deep ultraviolet spectral range," *Advanced Optical Materials*, vol. 4, no. 11, pp. 1780–1786, 2016.

[28] M. Daimon and A. Masumura, "Measurement of the refractive index of distilled water from the near-infrared region to the ultraviolet region," *Applied Optics*, vol. 46, no. 18, pp. 3811–3820, 2007.

[29] J. Munday, F. Capasso, V. A. Parsegian, and S. M. Bezrukov, "Measurements of the Casimir-Lifshitz force in fluids: The effect of electrostatic forces and debye screening," *Physical Review A*, vol. 78, no. 3, p. 032109, 2008.

[30] J. N. Munday, F. Capasso, and V. A. Parsegian, "Measured long-range repulsive Casimir-Lifshitz forces," *Nature*, vol. 457, no. 7226, pp. 170–173, 2009.

[31] A. Le Cunuder, A. Petrosyan, G. Palasantzas, V. Svetovoy, and S. Ciliberto, "Measurement of the Casimir force in a gas and in a liquid," *Physical Review B*, vol. 98, no. 20, p. 201408, 2018.

[32] L. B. Pires, D. S. Ether, B. Spreng, G. R. d. S. Araújo, R. S. Decca, R. Dutra, M. Borges, F. S. Rosa, G.-L. Ingold, M. J. Moura, *et al.*, "Probing the screening of the Casimir interaction with optical tweezers," *Physical Review Research*, vol. 3, no. 3, p. 033037, 2021.

[33] J. N. Munday and F. Capasso, "Precision measurement of the Casimir-Lifshitz force in a fluid," *Physical Review A*, vol. 75, no. 6, p. 060102, 2007.